

Retinal Microaneurysm Detection Through Local Rotating Cross-Section Profile Analysis

Istvan Lazar* and Andras Hajdu

Abstract—A method for the automatic detection of microaneurysms (MAs) in color retinal images is proposed in this paper. The recognition of MAs is an essential step in the diagnosis and grading of diabetic retinopathy. The proposed method realizes MA detection through the analysis of directional cross-section profiles centered on the local maximum pixels of the preprocessed image. Peak detection is applied on each profile, and a set of attributes regarding the size, height, and shape of the peak are calculated subsequently. The statistical measures of these attribute values as the orientation of the cross-section changes constitute the feature set that is used in a naïve Bayes classification to exclude spurious candidates. We give a formula for the final score of the remaining candidates, which can be thresholded further for a binary output. The proposed method has been tested in the Retinopathy Online Challenge, where it proved to be competitive with the state-of-the-art approaches. We also present the experimental results for a private image set using the same classifier setup.

Index Terms—Biomedical image processing, image classification, pattern recognition, medical decision-making.

I. INTRODUCTION

DIABETIC retinopathy (DR) is one of the complications of diabetes that develops in most of the patients with long-standing illness, and the leading cause of blindness in the developed countries [1]. Effective treatments for DR are available, though it requires early diagnosis and the continuous monitoring of diabetic patients. Diagnosis of DR is performed by the evaluation of retinal (fundus) images. Manual grading of these images to determine the severity of DR is rather slow and resource demanding [2]. The presence of microaneurysms (MAs) on the retina is the first and most characteristic symptom of this disease [3]. MAs on the retina appear as small, round shaped, red dots. Fig. 1 shows an example of a fundus image exhibiting signs of DR in terms of the appearance of MAs.

In this paper, we examine the problem of automated retinal MA detection, and propose a method for this task, which turned

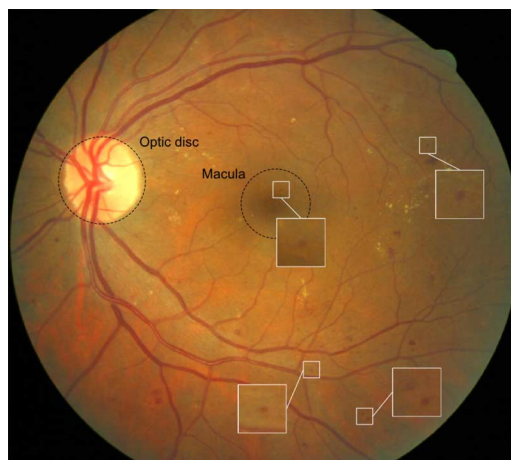


Fig. 1. An example of a fundus image showing signs of DR. Some MAs are zoomed.

out to be highly competitive with most of the state-of-the-art ones, based on the results of an open online competition. The recognition of MAs is essential in the process of DR grading, since it forms the basis of deciding whether an image of a patient's eye should be considered healthy or not. Therefore, it is not surprising that the literature on the aspects of developing a computer aided diagnostic (CAD) system for the detection of DR and other eye related diseases is rather extensive, and the analysis of retinal images is a very vivid field for the digital image processing community.

MAs have a clinically established maximal diameter, usually considered to be less than the diameter of the major optic veins. Crossings of thin blood vessels may result in small circular spots that are locally similar to MAs, both in size and shape. Vessel segments may be disconnected from the vascular tree, and appear as small, dark objects of various shapes.

Almost every state-of-the-art method considers some sort of image preprocessing step, which usually consists of noise reduction, filtering or shade correction. Retinal images have the largest contrast in the green channel; accordingly it is a common practice to use the green channel for segmentation purposes. For noise reduction, convolution with Gaussian masks and median filtering are widely applied methods.

The first computerized approaches for the segmentation of retinal MAs were described by Laÿ [4] and Baudoin *et al.* [5]. These methods calculate the maximum of morphological openings with linear structuring elements of different orientations. This step results in an image from which the structures that are smaller than the structuring element are missing. Therefore, the

Manuscript received September 21, 2012; revised November 06, 2012; accepted November 11, 2012. Date of publication November 21, 2012; date of current version January 30, 2013. This work was supported by the TÁMOP-4.2.2.C-11/1/KONV-2012-0001 project. The work was supported in part by the European Union, co-financed by the European Social Fund. This work was also supported in part by OTKA/NK101680—Mathematical modeling of clinical observations for improved melanoma detection. *Asterisk indicates corresponding author.*

*I. Lazar is with the Department of Informatics, University of Debrecen, 4010 Debrecen, Hungary (e-mail: lazar.istvan@inf.unideb.hu).

A. Hajdu is with the Department of Informatics, University of Debrecen, 4010 Debrecen, Hungary (e-mail: hajdu.andras@inf.unideb.hu).

Digital Object Identifier 10.1109/TMI.2012.2228665

difference of this image and the original one (top-hat transformation) may be thresholded to obtain MA candidates. These approaches have constituted the basis for several later algorithms. We also note that Zana *et al.* [6] applied the same morphological approach for retinal vessel segmentation.

In [7], Spencer *et al.* applied preceding illumination and shade correction steps to improve the quality of the fluorescein angiography images before the actual segmentation and detection steps. A Gaussian match filter was used after the bilinear top-hat transformation to enhance MA like objects, and a recursive region growing method produced the segmented MA candidates. This was the first method that applied an additional classification step, that is, supervised learning based methods are used to filter out spurious candidates. For this aim, a set of features are calculated for each candidate. These features are intended to capture those characteristics that help to distinguish true candidates from false ones, since the first step usually results in a high number of possible candidates. Variations of this method with different preprocessing steps and classification methods have been proposed by several authors, e.g., Cree *et al.* [8], Frame *et al.* [9], Mendonca *et al.* [10], and Fleming *et al.* [11].

A limitation of the morphological approach by Laÿ [4] is that the usage of too large structuring elements would result in the detection of tight vessel curvings as possible MAs. However, if the length of the linear structuring element is chosen so that no parts of the vasculature will be wrongly detected, true MAs will be lost, since no circular structure that is larger than the structuring element can be detected in this way. In [12], the authors considered an additional pixelwise classification based candidate extraction method, and merged the output. Other morphology based methods include the one proposed by Walter *et al.* [13], in which criteria based morphology operators [14] are applied in the candidate extraction phase followed by the candidate classification. Ram *et al.* [15] proposed a method in which the candidate selection is the same as described in [12], and a two-stage candidate rejection step is applied. The score of the remaining candidates are calculated as their distance from the optimal hyperplane of a support vector machine.

Nonmorphology based methods have also been investigated. Zhang *et al.* [16] used Gaussian masks of different size and standard deviation, and calculated the maximal pixelwise correlation with the original image. The result produced the basis of the candidate extraction phase, and the values were also used in the candidate classification step. Mizutani *et al.* [17] utilized a double-ring filter for the initial detection of MAs. Quéllec *et al.* proposed an approach using template matching in the wavelet domain [18]. In the method proposed by Sanchez *et al.* [19] the histogram of the preprocessed image is modeled using a three-component mixture model, assuming normal distribution of the gray level of each class. The MA candidates are extracted by thresholding the obtained model, and classified by a logistic regression classifier.

The method we propose in this paper realizes the detection of MAs through the analysis of the intensity values along discrete line segments of different directions centered at the candidate pixel. These profiles are referred to as cross-section or intensity profiles. In a previous work we have shown how this prin-

ciple can be utilized to unsupervised MA detection [20], which technique proved to be competitive with many state-of-the-art ones in an open online competition. The method proposed in this paper considers an entirely different approach by dividing the detection process into the steps of candidate extraction, feature extraction, classification, and score determination. The results of the proposed method in the same online competition proved that it is not just able to remarkably outperform its predecessor, but it turned out to be the best nonensemble based MA detector among all participants.

Methods with similar principle for retinal vessel segmentation have also been proposed by several authors. In [21], features extracted from profiles perpendicular to the assumed vessel regions are considered, and in [22], the cross-section of a vessel is represented in the Fourier domain. In [23], Ricci *et al.* consider lines of fixed length passing through the target pixel at different orientations in order to detect segments of the vasculature. The MA detection method proposed by Giancardo *et al.* in [24] is based on Radon transformation with a similar theoretical background. In [23], the authors propose a similar cross-sectional approach for vessel segmentation, and the 2D “tramline” filter proposed by Lowell *et al.* in [25] is also discussed, with the conclusion that it is suitable for vessel centerline detection.

The rest of this paper is structured as follows. In Section II, the steps of the proposed approach are described in details. In Section III, the methodology of performance evaluation and the experimental results are given. We summarize the main points and draw conclusions in Section IV with discussing the possible future applications of the proposed method, as well.

II. PROPOSED METHOD

The main input of the proposed method is the inverted green channel of a fundus image, since this way MAs, hemorrhages, and the vasculature will appear as bright structures, i.e., local intensity maximum regions. We also consider the binary region of interest (ROI) mask. Several methods exist to detect the ROI, e.g., the one proposed by Gagnon *et al.* [26]. We require the input images to have such spatial resolution that the diameter of their ROI is equal to 540 pixels, since this was the smallest ROI diameter we came across in the publicly available fundus image sets. Naturally, it is possible to apply the proposed method on images of different size, though in this case other parameters of the proposed method have to be altered accordingly, and the more image data results in longer execution time. We applied bilinear interpolation in our implementation to calculate the intensity values of the rescaled images. For the better understanding of the proposed method, its schematic workflow is shown in Fig. 2.

A. Image Preprocessing

The proposed method does not require a specific preprocessing step, however, we found that it is beneficial to consider a certain amount of image smoothing before the actual steps of detection. This is partially due to the fact that many fundus images are available in a lossy compressed format, resulting in the distortion of small structures such as MAs. Since the proposed method particularly relies on the local intensity distribution of

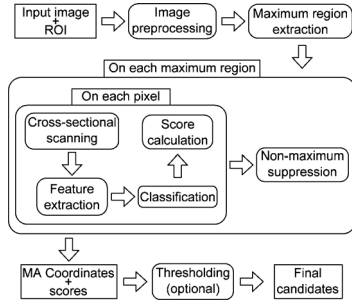


Fig. 2. Workflow of the proposed method.

MAs, it is important to reduce the effect of noise. In our implementation, we applied convolution with a Gaussian mask with a variance of 1.0. Our experiments showed that this amount of smoothing suppressed noise sufficiently while preserving true MAs. Other image enhancement techniques could also be considered; it is possible that images from other sources than those we discuss in this paper may require different preprocessing.

B. Local Maximum Region Extraction

MAs are local intensity maximum structures on the preprocessed retinal image, usually with a Gaussian like intensity distribution. This means that every MA region contains at least one regional maximum also. A local maximum region (LMR), of a grayscale (intensity) image is a connected component of pixels with a given constant intensity value, such that every neighboring pixel of the region has a strictly lower intensity [27]. Therefore, it is sufficient to consider only the LMRs of the preprocessed image as possible MA candidate regions. In our implementation, we applied a simple breadth-first search algorithm, similar to the one described in [27] for the calculation of grayscale morphological reconstruction. Pixels of the image are processed sequentially, and compared to their 8-neighbors. If all neighbors have a lower intensity, then the pixel itself is a LMR. If there is a neighboring pixel with higher intensity, then the current pixel may not be a maximum. A pixel is considered to be a possible maximum if all neighboring pixels have lower or the same intensity, in which case pixels with the same intensity are stored in a queue, and tested in the same way. If eventually the queue is emptied so that all the pixels it contained proved to be possible maxima, then the corresponding connected component is a LMR.

Pixels of a LMR are considered individually as possible candidates, and the pixel with the maximum final score will represent the region; this procedure is referred to as nonmaximum suppression, and it will be discussed in details later on. We note that the usage of image smoothing, as discussed in the previous section, gains importance at this point, since the local intensity variations may be high on a raw retinal image, resulting in many local maxima.

C. Cross-Sectional Scanning

To examine the surrounding of a single maximum pixel in a MA candidate region, the intensity values along discrete line segments of different orientations, whose central pixel is the

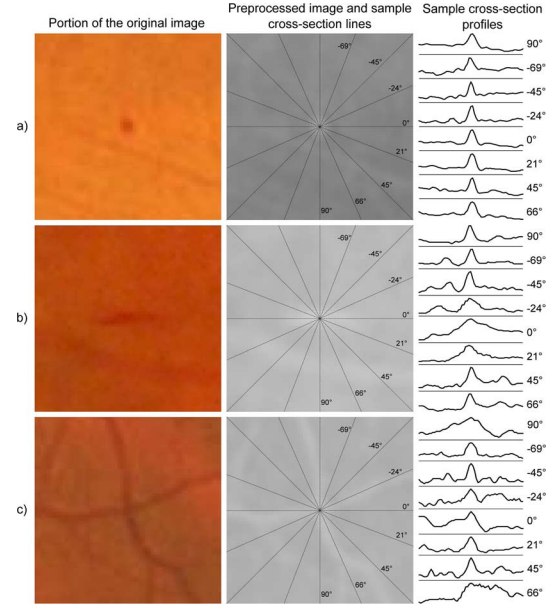


Fig. 3. Sample cross-section profiles of an MA (a), an elongated non-MA object (b), and a vessel crossing (c), respectively.

candidate pixel, are recorded. In this way, we obtain a set of cross-sectional intensity profiles.

Similar procedure is described in [23] as a basic line detector. The authors reported that they achieved the best performance with lines of length 15 pixels, with also referring to the method proposed in [6], where line operators of the same length are used as structuring elements for vessel segmentation. However, while in that case the average intensity along the line is considered, we will use the resulting intensity profiles to detect and measure the properties of a central peak on it, if present. Due to this fact, it is not that critical to find an optimal length for the cross-section lines, though it has to be sufficiently large to enable the distinction of MAs from hemorrhages and parts of the vasculature. Hence, in our implementation, the length of the cross-sections was chosen to be 31 based on our experiments. The authors in [23] mention a 15° angular resolution for the rotation of the line segments. We experimentally found that a 6° difference between the consecutive cross-sections is more adequate, since we consider larger cross sections. The number of resulting profiles can be easily calculated as $180^\circ/\alpha$, where α denotes the *scan step*, i.e., we consider 30 cross sections.

Fig. 3 shows sample cross sections of an MA, a vessel crossing, and an elongated non-MA structure. The orientations of the sample cross sections were chosen so that the differences between the objects are best shown. As it can be seen, MAs show a definite Gaussian like peak for all directions, opposed to other noncircular structures.

D. Peak Detection and Property Measurement on the Cross-Section Profiles

On the obtained cross-section profiles we perform a peak detection step. Our aim is to decide whether a peak is present at the center of the profile, i.e., at the location of the candidate point for a specific direction. We calculate several properties of the peak, and the final feature set consists of a set of statistical

measures that show how these values vary as the orientation of the cross-section is changing. This way, the variation of important characteristics, such as symmetry and shape of the structure, and its difference from the background may be numerically expressed.

The detection of peaks in one dimensional discrete data is a common issue in many fields of science, such as the automatic evaluation of spectrometric [28], [29], chromatographic [30], [31], and cardiographic data. It also has a wide range of applications in signal processing. Localizing peaks in image histograms is used in many cases, e.g., for image segmentation or quantization. The applied methods are of many kinds and usually they are the most suitable for a specific problem, though the expectations towards a method also vary among the applications. The methods available in the literature consider e.g., template matching, wavelet transformation, statistical approaches, baseline corrections, thresholding.

The basis of the peak detection method we apply is to locate strictly monotonic segments (ramps) of the profile. Let P denote a profile and $P[i]$ its i th value. A ramp is defined as a segment of the profile, i.e., $(P[m], P[m+1], \dots, P[n])$ where the sign of the difference between the consecutive values is nonzero, and the same along the segment, i.e., $\text{sgn}(P[i] - P[i-1]) = \text{sgn}(P[i+1] - P[i])$ for every $m < i < n$. Additionally, the absolute difference between consecutive values should not be less than parameter min_diff , and the height of the ramp, i.e., the absolute difference between the first and last value should be not less than parameter min_height , either. The value of min_diff acts as a lower threshold for the slope of the ramps, and it controls how sharp the intensity transition should be. The purpose of the min_height parameter is to give a lower noise threshold. Based on whether $\text{sgn}(P[i+1] - P[i])$ is positive or negative, the ramps are considered to be increasing or decreasing ramps, respectively. We have examined the cross-section profiles of several MAs, and found that by setting min_diff to 2, and the min_height to 3, small monotonic segments that are clearly noise artifacts can be eliminated.

Once the ramps are located, it is tested, whether there is a full peak at the center of the profile, i.e., the ramp left to the central index is increasing, and the one on the right is decreasing. Since only maximum regions are considered as candidates, it is not possible that the central index of the profile is inside a ramp; however, it may be the end or the start of a ramp. In addition, increasing ramps on the left, and decreasing ramps on the right of the peak are successively attached as long as the gap between two consecutive ramps is not greater than a fixed value max_gap . This way, a more noise and local intensity variation tolerant peak detection can be achieved. In our implementation, we set this value to 3, which we also determined based on our observations, as also in the case of the min_diff and min_height parameters. The final peak is represented by four descriptive values: inc_s , inc_e , dec_s , and dec_e . The values of inc_s and inc_e correspond to the start and end indices of the increasing ramp, the same way as dec_s and dec_e denote the boundaries of the decreasing ramp, respectively. Fig. 4 shows a graphical interpretation of the ramps (a) on a sample cross-section profile, and how the full peak is formed (b).

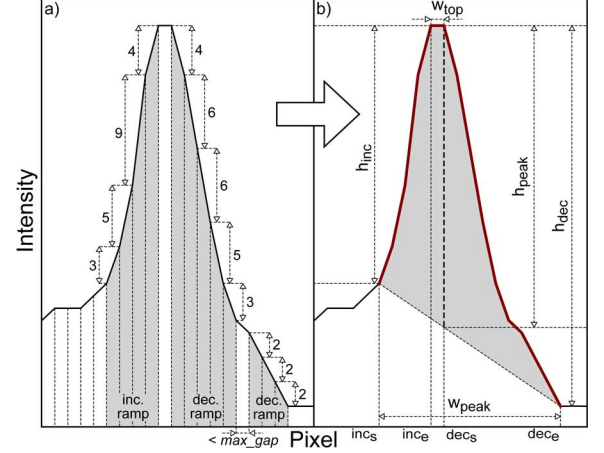


Fig. 4. Increasing and decreasing ramps on a sample profile (a), and the result of the peak detection and the calculated peak measures (b).

Once a peak is detected at the center of a profile P , the following properties are calculated.

- 1) The *peak width* is the difference between the start and end indices of the peak: $w_{\text{peak}} = \text{dec}_e - \text{inc}_s$.
- 2) The *top width* is the size of the gap between the increasing and decreasing ramp: $w_{\text{top}} = \text{dec}_s - \text{inc}_e$.
- 3) The *increasing ramp height*: $h_{\text{inc}} = P[\text{inc}_e] - P[\text{inc}_s]$.
- 4) The *decreasing ramp height*: $h_{\text{dec}} = P[\text{dec}_s] - P[\text{dec}_e]$.
- 5) The *increasing ramp slope*: $s_{\text{inc}} = h_{\text{inc}} / (\text{inc}_e - \text{inc}_s)$.
- 6) The *decreasing ramp slope*: $s_{\text{dec}} = h_{\text{dec}} / (\text{dec}_e - \text{dec}_s)$.
- 7) The *peak height* is calculated as the difference between the intensity of the central pixel and a baseline that connects the start and end of the profile: $h_{\text{peak}} = P[\text{center}] - (P[\text{dec}_e] - P[\text{inc}_s]) / w_{\text{peak}} \cdot (\text{center} - \text{inc}_s) + P[\text{inc}_s]$.

The value of *peak width* corresponds to the extension of the structure in the considered direction. The *top width* measures how large the maximum area in the structure is. The heights and slopes of the increasing and decreasing ramps provide information about the distinction from the surroundings, and the sharpness of the intensity transition. We note that the slope is considered to be positive for decreasing ramps, too. The *peak height* value combines the heights of the increasing and decreasing ramps by fitting a baseline to the peak, and calculating the central pixels distance from it. The calculated peak measures—except the slopes—on the previous sample cross-section profile are shown in Fig. 4(b).

E. Feature Set and Classification

After the cross-sectional scanning and peak detection steps are performed for every scan direction on a given candidate, we calculate several statistical measures of the resulting directional peak properties. For better understanding, we define five sets that contain the values of the corresponding peak properties as obtained on all scan directions. The *increasing-* and *decreasing ramp height* values are stored in the *RHEIGHTS* set, likewise, the *ramp slope* values are stored in *RSLOPES*. The *TWIDTHS*, *PWIDTHS*, and *PHEIGHTS* sets contain the *top width*, *peak width*, and *peak height* values,

respectively. Let μ_T , σ_T , and cv_T denote the respective mean, standard deviation and coefficient of variation of the values in set T , where the coefficient of variation is the ratio of the standard deviation and the mean, i.e., $cv = \sigma/\mu$. We consider the following feature set for classification: $F = \{\mu_{PWIDTHS}, \sigma_{PWIDTHS}, \mu_{TWIDTHS}, \sigma_{TWIDTHS}, \sigma_{RSLOPES}, cv_{RHEIGHTS}, cv_{PHEIGHTS}\}$. The value of $\mu_{PWIDTHS}$ gives a good measure of the extension of the candidate object, and $\sigma_{PWIDTHS}$ shows how symmetric it is. $\mu_{TWIDTHS}$ and $\sigma_{TWIDTHS}$ serve a similar purpose by describing the inner region of the candidate. $\sigma_{RSLOPES}$ has a higher value for vessel crossings. The $cv_{RHEIGHTS}$ and $cv_{PHEIGHTS}$ values provide normalized measures of the variations in the sharpness of the contour. Using this feature set we are able to distinguish MAs from the most common interfering objects, such as small disconnected vessel fragments, vessel crossings and bifurcations, retinal hemorrhages that are only slightly larger than MAs, or local darkenings on the vessels.

For classification, we used a naïve Bayes (NB) classifier, a simple and robust probabilistic algorithm that assumes the individual features to be independent. The training set consists of both positive and negative MA examples. Usually, it is rather straightforward to obtain the feature vectors of positive instances of the training set, since in most public datasets the coordinates of MAs on the images are given. The non-MA set consists of the previously described most common false positives. The training of a NB classifier means the estimation of the class priors and feature probability distributions. Following the common practice when dealing with continuous data, we assume that the feature values in each class are of Gaussian distribution. This also means that the parameters of the distribution can be estimated using the sample means and variances of the training data for the given feature. We also consider the class priors to be equal. We have tested other classification methods, such as k-nearest neighbor (kNN), and support vector machines (SVMs) with different kernel functions, as well. Our experiments showed that there was only a minimal difference in the final performance, but NB gave a slightly better result. Besides, its low computational time and its robustness are also advantageous. However, it is not our intention to find the most suitable classification method, much rather to show the ability of the proposed feature set to express the important characteristics of MAs.

The training set, different classifier results and the performance evaluation methodology will be discussed in details in the experimental results section.

F. MA Score Calculation and Nonmaximum Suppression

To meet the requirements of a real-life DR screening system, score values are assigned to the MA candidates that were

classified as true MAs, which score considers the shape, symmetry, sharpness and contrast of the candidate. The score is constructed in such a way that stronger, more visible MAs achieve higher score than faint ones. We found that the minimal value of $PHEIGHTS$, i.e., $\min_{PHEIGHTS}$ is more expressive considering the distinctiveness of the candidate than e.g., the mean would be, and its product with μ_{SLOPES} gives a good measure of how strongly-appearing the structure is. The MA score is calculated using the formula shown at the bottom of the page. The score calculated this way will be maximal, when the variables in the denominator equal zero, and it assigns higher score to locally more distinctive candidates with sharper edges, while taking into consideration that variation in the important features should be as low as possible. We note that instead of the coefficient of variation of $RHEIGHTS$ and $PHEIGHTS$ the standard deviations are considered.

The final step of the proposed method is the nonmaximum suppression. We have described earlier that in the case of regional maxima, all points of the region are considered as candidate pixels. Nonmaximum suppression at this point refers to the operation of selecting the point with the highest score from every maximum region that will represent the corresponding candidate. Therefore, points with nonmaximal score in a candidate region are neglected, and the output of the proposed method is a set of coordinates and the corresponding score values. We note that the MA scores are not normalized values. Optionally, it is possible to have a binary output for the MA candidates with an appropriate thresholding of the score values.

III. EXPERIMENTAL RESULTS

A. Performance Evaluation Methodology

The most widespread technique for the performance evaluation of abnormality detection methods in medical images is the usage of free-response ROC (FROC) curves. A FROC curve plots sensitivity (the proportion of true positive detections) against the average number of false positives per image. Since the FROC curve does not depend on the number of true negative points on the image, it is suitable to compare the performance of detection methods that provide an unknown number of candidates, presumably corresponding to abnormalities on an image. Since there is no upper limit of the right side of a FROC curve, i.e., the average number of false positives per image can be theoretically infinite, no widely accepted index number that describes an entire FROC curve exists. In this paper, by following the evaluation protocol of the Retinopathy Online Challenge as described in the next section, we consider a score value that is calculated as the average sensitivity at seven false positive rates.

The proposed method has been tested on two independent datasets: in an open online competition and on a private image

$$\text{score} = \frac{\min_{PHEIGHTS} \cdot \mu_{RSLOPES}}{1 + \sigma_{PWIDTHS} + \sigma_{TWIDTHS} + \sigma_{RSLOPES} + \sigma_{RHEIGHTS} + \sigma_{PHEIGHTS}}$$

TABLE I
MEANS AND STANDARD DEVIATIONS OF THE TRAINING FEATURE VECTORS

| Feature | MA | non-MA |
|--------------------|---------------------|----------------------|
| $\sigma_{RSLOPES}$ | 0.7623 ± 0.1280 | 1.2522 ± 0.6934 |
| $CVPHEIGHTS$ | 0.1989 ± 0.2407 | 0.3329 ± 0.0476 |
| $CVRHEIGHTS$ | 0.2594 ± 0.0375 | 0.4389 ± 0.0369 |
| $\mu_{TWIDTHS}$ | 1.2095 ± 7.3803 | 1.7283 ± 3.3291 |
| $\sigma_{TWIDTHS}$ | 0.7459 ± 1.3820 | 1.6078 ± 2.4946 |
| $\mu_{PWIDTHS}$ | 8.5987 ± 7.0796 | 11.7989 ± 7.5289 |
| $\sigma_{PWIDTHS}$ | 1.8159 ± 1.1965 | 3.7547 ± 2.7767 |

set which was provided by the Moorfields Eye Hospital, U.K. No additional vessel or optic disc detection was applied.

B. Retinopathy Online Challenge

The Retinopathy Online Challenge (*ROC*) [32] is an international online competition dedicated to compare the accuracy of microaneurysm detectors under the same conditions. The publicly available dataset consists of 50 training and 50 test images, but the location of the MAs is only available for the test set. This gives each participating team the opportunity to train their methods on the training set, and submit their results obtained on the test set, in the form of pairs of candidate coordinates and confidence values. The final score of a method is calculated as the average sensitivity at seven false positive rates (1/8, 1/4, 1/2, 1, 2, 4, and 8 false positives per image).

The proposed method applies a two-class classification; therefore, it requires two sets of training examples. Assembling the positive (MA) set is rather straightforward. However, compilation of the negative (non-MA) set is more complicated, since its elements have to be selected manually. To construct the training feature set for the classifier of the proposed method, we took the official marking of the MAs on the training set as a basis, and we sorted out the ambiguous ones manually. The non-MA set consisted mostly of vessel crossings and bifurcations, elongated disconnected vessel fragments and haemorrhages. Table I shows the means and standard deviations of the feature values for the two classes in the training data. Moreover, these values constitute the configuration of the applied naïve Bayes classifier. To decide which classification method should be used, we tested the proposed method on the training set, since the MA markings are not available for the test set. Using NB classifier, a score of 0.1509 was achieved, while scores in the cases of a kNN ($k = 15$) and an SVM with radial basis function kernel (libSVM default setting) were 0.1500 and 0.1490, respectively. The difference between the considered classifiers is obviously minimal; speed and robustness were also in the favor of choosing NB.

The proposed method achieved an overall score of 0.423, as evaluated by the *ROC* organizers, which currently ranks it at the second place among all the submitted methods. The first placed method [33] is an ensemble-based one, which combines several individual algorithms, including our previous one [20], as well. While its average FROC score is slightly higher, it is important to mention that the proposed method achieved higher sensitivity at low false positive rates, i.e., 1/8 and 1/4 FPs/image. The FROC curve of the proposed method can be seen in Fig. 5,

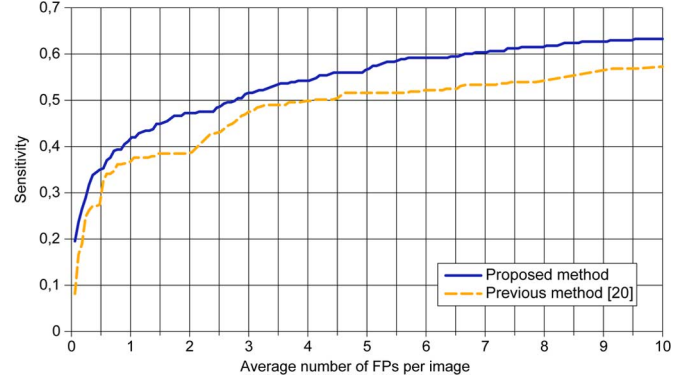


Fig. 5. FROC curve of the proposed method, based on its result in the ROC competition. The curve of our previous method in the same competition is also shown.

TABLE II
PARTICIPATING TEAMS IN THE *ROC*, AND THEIR ACHIEVED SCORES

| | Team name | Score |
|-----|---|--------------|
| 1. | DRSCREEN [33] | 0.434 |
| 2. | Lazar et al. (the proposed method) | 0.423 |
| 3. | Z. Fegyver | 0.422 |
| 4. | Niemeijer et al. [12] | 0.395 |
| 5. | LaTIM [18] | 0.381 |
| 6. | ISMV [24] | 0.375 |
| 7. | OKmedical II. | 0.369 |
| 8. | OKmedical [16] | 0.357 |
| 9. | Lazar et al. (Our previous method) [20] | 0.355 |
| 10. | GIB Valladolid [19] | 0.322 |
| 11. | Fujita Lab [17] | 0.310 |
| 12. | IRIA-Group [15] | 0.264 |
| 13. | Waikato Retinal Imaging Group | 0.206 |

TABLE III
SENSITIVITIES AT THE PREDEFINED FALSE POSITIVE PER IMAGE RATES FOR THE PROPOSED METHOD AND THE FIRST PLACED ENSEMBLE BASED ONE IN THE *ROC*

| | 1/8 | 1/4 | 1/2 | 1 | 2 | 4 | 8 |
|---------------------|--------------|--------------|-------|-------|-------|-------|-------|
| The proposed method | 0.251 | 0.312 | 0.350 | 0.417 | 0.472 | 0.542 | 0.615 |
| DRSCREEN [33] | 0.173 | 0.275 | 0.380 | 0.444 | 0.526 | 0.599 | 0.643 |

along with the curve of the previous method of ours, which individually achieved the score 0.3548. Table II summarizes the participating teams in the *ROC*, along with their achieved scores. We note that the methods cited in Table II are discussed in details in the introduction section of this paper. Table III shows the sensitivities at the seven predefined false positive rates for the proposed method and the first placed ensemble-based one.

C. Moorfields Eye Hospital Dataset

Besides the *ROC* competition, we have tested the proposed method on another dataset, which was provided by the Moorfields Eye Hospital, London, U.K. This dataset consists of 60 retinal images, and the coordinates of the MA centroids are also given. The FOV of the images is 45° , and the diameter of the ROI is approximately 2200 pixels. In order to evaluate the proposed method on this dataset, we used the same classifier setup as for the *ROC*, and hereby, we were able to test on all 60 images without splitting it into a training and test set. Opposite to the evaluation protocol of the *ROC*, where certain

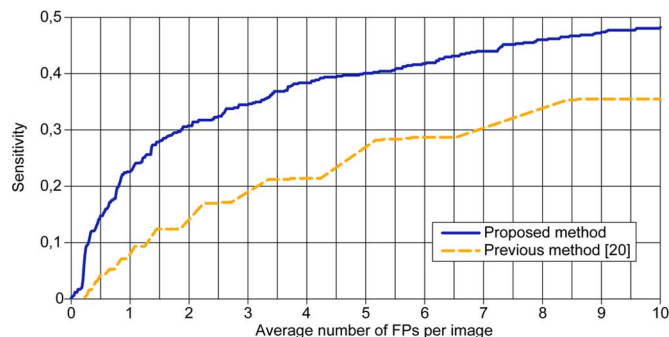


Fig. 6. FROC curve of the proposed method and its predecessor on the image set provided by the Moorfields Eye Hospital, London, U.K.

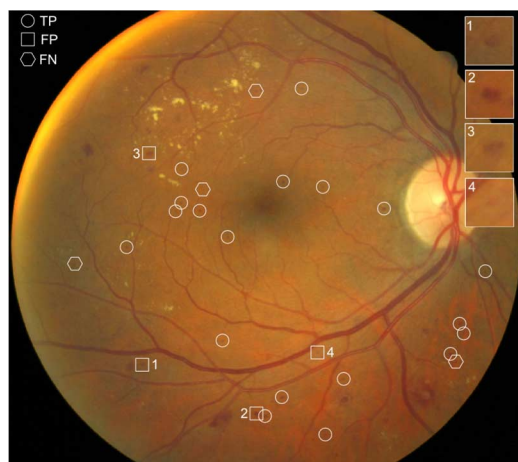


Fig. 7. Image showing the result of the detection in the Moorfields Eye Hospital dataset. Four false positive detections are highlighted.

lesions were labeled as “irrelevant,” and hence their detection was not counted as a false positive, in the case of the annotation of these images no such category exists, which results in a lower sensitivity at the same false positive rate, compared to the *ROC*. We have also tested our previous method in these images, and as in the case of the *ROC*, the proposed method achieved higher sensitivity at every false positive rate, proving its robustness in a scenario, where there is no possibility to repeatedly retrain the method on every new image set. The score of the proposed method was 0.233 on this dataset, while our previous method achieved 0.117. Fig. 6 shows the FROC curve of the proposed and our previous method, respectively. An image from this dataset is shown in Fig. 7, with the true positive (TP), false positive (FP), and false negative (FN) detections are highlighted, while the four false positives are shown in details. The score threshold was chosen so that the number of average false positives per image was 2.

D. Execution Time and Implementation Details

The proposed method was implemented entirely in Java SE 1.6. The average computational time of an image was approximately 2 s, without parallelization, using a PC with an Intel Core2 Quad Q8200 Processor and 2 GB RAM. For comparison, the average processing time of our previous method was approximately 15 s, taking advantage of parallelization. This increase in speed is due to the lower number of candidate pixels, the fast



Fig. 8. Parts of the vasculature and artifacts on the optic disc that locally appear as MAs.

feature extraction and classification, and the simple final score calculation.

IV. CONCLUSION AND FURTHER WORK

In this paper, we have presented a method for the detection of MAs on retinal images, based on the principle of analyzing directional cross-section profiles centered on the candidate pixels of the preprocessed image. The number of pixels to be processed is significantly reduced by only considering the local maxima of the preprocessed image. We apply peak detection on each profile, and calculate a set of values that describe the size, height, and shape of the central peak. The statistical measures of these values as the orientation of the cross-section changes constitute the feature set used in a classification step to eliminate false candidates. We proposed a formula to calculate the final score of the remaining candidates based on the obtained feature values.

The proposed method has been evaluated in the Retinopathy Online Challenge (*ROC*), where it achieved higher score than any other individual method, and the only higher score was achieved by an ensemble based method that includes the predecessor of the proposed one. However, the proposed method achieved higher sensitivity at low false positive rates, i.e., at 1/8 and 1/4 FPs/image. Besides this open online challenge, we have also tested the method on a private dataset, on which it also significantly outperformed its predecessor. Instead of splitting the dataset containing 60 color fundus images into a training and a test subset, we used the classifier setup obtained on the *ROC* training set, which proves the robustness of the proposed method. The fact that the performance difference between the currently proposed and our previous method in this case was even higher than in the *ROC* confirms again its tolerance against noise corruption from different image sources. The processing time is also rather favorable with an average 2 s per image.

We did not apply any additional vessel or optic disk detection step. The proposed method proved to be able to distinguish vessel bifurcations and crossings from MAs rather well; however, some of the false positives come from the region of the optic disc. As it can be seen on Fig. 8, MA-like structures do appear on the optic disc, and since the contrast is very high in this region, sometimes a rather high score is assigned. Though the proposed method showed convincing performance, this could probably be further improved by adding an optic disc detection step and excluding MA detections within this region.

We believe that the proposed cross-section analysis based feature extraction and feature set could be exploited in other medical image processing related tasks, especially in cases of abnor-

ality detection that involve the recognition of nearly circular or slightly elongated structures in an image.

REFERENCES

- [1] R. Klein, B. E. K. Klein, and S. E. Moss, "Visual impairment in diabetes," *Ophthalmology*, vol. 91, pp. 1–9, 1984.
- [2] P. J. Kertes and T. M. Johnson, Eds., *Evidence Based Eye Care*. Philadelphia, PA: Lippincott Williams & Wilkins, 2007.
- [3] Early Treatment Diabetic Retinopathy Study Research Group, "Early photocoagulation for diabetic retinopathy," *Ophthalmology*, vol. 98, pp. 766–85, 1991.
- [4] B. Lay, "Analyse automatique des images angiofluorographiques au cours de la retinopathie diabétique," Ph.D. dissertation, Centre of Mathematical Morphology, Paris School of Mines, Paris, France, 1983.
- [5] C. E. Baudoin, B. J. Lay, and J. C. Klein, "Automatic detection of microaneurysms in diabetic fluorescein angiographies," *Rev. Epidemiol Sante Publique*, vol. 32, pp. 254–261, 1984.
- [6] F. Zana and J. C. Klein, "Segmentation of vessel-like patterns using mathematical morphology and curvature evaluation," *IEEE Trans. Image Process.*, vol. 10, no. 7, pp. 1010–1019, Jul. 2001.
- [7] T. Spencer, J. A. Olson, K. C. McHardy, P. F. Sharp, and J. V. Forrester, "An image-processing strategy for the segmentation and quantification of microaneurysms in fluorescein angiograms of the ocular fundus," *Comput. Biomed. Res.*, vol. 29, pp. 284–302, May 1996.
- [8] M. J. Cree, J. A. Olson, K. C. McHardy, P. F. Sharp, and J. V. Forrester, "A fully automated comparative microaneurysm digital detection system," *Eye*, vol. 11, pp. 622–628, 1997.
- [9] A. J. Frame, P. E. Undrill, M. J. Cree, J. A. Olson, K. C. McHardy, P. F. Sharp, and J. Forrester, "A comparison of computer based classification methods applied to the detection of microaneurysms in ophthalmic fluorescein angiograms," *Comput. Biol. Med.*, vol. 28, pp. 225–238, 1998.
- [10] A. Mendonca, A. Campilho, and J. Nunes, "Automatic segmentation of microaneurysms in retinal angiograms of diabetic patients," in *Proc. Int. Conf. Image Anal. Process.*, 1999, pp. 728–733.
- [11] A. D. Fleming, S. Philip, and K. A. Goatman, "Automated microaneurysm detection using local contrast normalization and local vessel detection," *IEEE Trans. Med. Imag.*, vol. 25, no. 9, pp. 1223–1232, Sep. 2006.
- [12] M. Niemeijer, J. Staal, M. D. Abramoff, M. A. Suttorp-Schulten, and B. van Ginneken, "Automatic detection of red lesions in digital color fundus photographs," *IEEE Trans. Med. Imag.*, vol. 24, no. 5, pp. 584–592, May 2005.
- [13] T. Walter, P. Massin, A. Arginay, R. Ordonez, C. Jeulin, and J. C. Klein, "Automatic detection of microaneurysms in color fundus images," *Med. Image Anal.*, vol. 11, pp. 555–566, 2007.
- [14] L. Vincent, "Morphological area openings and closings for greyscale images," in *Proc. NATO Shape Picture Workshop*, 1992, pp. 197–208.
- [15] K. Ram, G. D. Joshi, and J. Sivaswamy, "A successive clutter-rejection-based approach for early detection of diabetic retinopathy," *IEEE Trans. Biomed. Eng.*, vol. 58, no. 3, pp. 664–673, Mar. 2011.
- [16] B. Zhang, X. Wu, J. You, Q. Li, and F. Karray, "Detection of microaneurysms using multi-scale correlation coefficients," *Pattern Recognit.*, vol. 43, no. 6, pp. 2237–2248, 2010.
- [17] A. Mizutani, C. Muramatsu, Y. Hatanaka, S. Suemori, T. Hara, and H. Fujita, "Automated microaneurysm detection method based on double ring filter in retinal fundus images," in *Proc. SPIE Med. Imag. 2009: Comput.-Aided Diagnosis*, 2009, vol. 72601N.
- [18] G. Quellec, M. Lamard, P. Josselin, G. Cazuguel, B. Cochener, and C. Roux, "Optimal wavelet transform for the detection of microaneurysms in retina photographs," *IEEE Trans. Med. Imag.*, vol. 27, no. 9, pp. 1230–1241, Sep. 2008.
- [19] C. I. Sanchez, R. Hornero, A. Mayo, and M. Garcia, "Mixture model based clustering and logistic regression for automatic detection of microaneurysms in retinal images," in *Proc. SPIE Med. Imag. 2009: Comput.-Aided Diagnosis*, 2009, vol. 72601M.
- [20] I. Lazar and A. Hajdu, "Microaneurysm detection in retinal images using a rotating cross-section based model," in *IEEE Int. Symp. Biomed. Imag.: From Nano to Macro*, 2011, pp. 1405–1409.
- [21] J. Staal, M. D. Abramoff, M. Niemeijer, M. A. Viergever, and B. Van Ginneken, "Ridge based vessel segmentation in color images of the retina," *IEEE Trans. Med. Imag.*, vol. 23, no. 4, pp. 501–509, Apr. 2004.
- [22] T. Zhu, "Fourier cross-sectional profile for vessel detection on retinal images," *Comput. Med. Imag. Grap.*, vol. 34, pp. 203–212, 2010.
- [23] E. Ricci and R. Perfetti, "Retinal blood vessel segmentation using line operators and support vector classification," *IEEE Trans. Med. Imag.*, vol. 26, no. 10, pp. 1357–1365, Oct. 2007.
- [24] L. Giancardo, F. Meriaudeau, T. P. Karnowski, Y. Li, K. W. Tobin, and E. Chaum, "Microaneurysm detection with radon transform-based classification on retina images," in *Proc. IEEE Annu. Int. Conf. EMBC*, 2011, pp. 5939–5942.
- [25] J. Lowell, A. Hunter, D. Steel, A. Basu, R. Ryder, and R. L. Kennedy, "Measurement of retinal vessel widths from fundus images based on 2-D modeling," *IEEE Trans. Med. Imag.*, vol. 23, no. 10, pp. 1196–1204, Oct. 2004.
- [26] L. Gagnon, M. Lalonde, M. Beaulieu, and M. C. Boucher, "Procedure to detect anatomical structures in optical fundus images," in *Proc. SPIE Med. Imag.: Image Process.*, 2001, vol. 4322, pp. 1218–1225.
- [27] L. Vincent, "Morphological grayscale reconstruction in image analysis: Applications and efficient algorithms," *IEEE Trans. Image Process.*, vol. 2, pp. 176–201, Apr. 1993.
- [28] K. H. Jarman, D. S. Daly, K. K. Anderson, and K. L. Wahl, "A new approach to automated peak detection," *Chemometr. Intell. Lab.*, vol. 69, pp. 61–76, 2003.
- [29] K. R. Coombes, S. Tsavachidis, J. S. Morris, K. A. Baggerly, M. C. Hung, and H. M. Kuerer, "Improved peak detection and quantification of mass spectrometry data acquired from surface-enhanced laser desorption and ionization by denoising spectra with the undecimated discrete wavelet transform," *Proteomics*, vol. 5, pp. 4107–4117, 2005.
- [30] G. Vivó-Truyols, J. R. Torres-Lapasió, A. M. Van Nederkassel, Y. Vander Heyden, and D. L. Massart, "Automatic program for peak detection and deconvolution of multi-overlapped chromatographic signals part I: Peak detection," *J. Chromatogr. A*, vol. 1096, pp. 133–145, 2005.
- [31] S. Peters, G. Vivó-Truyols, P. J. Marriott, and P. J. Schoenmakers, "Development of an algorithm for peak detection in comprehensive two-dimensional chromatography," *J. Chromatogr. A*, vol. 1156, pp. 14–24, 2007.
- [32] M. Niemeijer, B. van Ginneken, M. Cree, A. Mizutani, G. Quellec, C. Sanchez, B. Zhang, R. Hornero, M. Lamard, C. Muramatsu, X. Wu, G. Cazuguel, J. You, A. Mayo, Q. Li, Y. Hatanaka, B. Cochener, C. Roux, F. Karray, M. Garcia, H. Fujita, and M. Abramoff, "Retinopathy online challenge: Automatic detection of microaneurysms in digital color fundus photographs," *IEEE Trans. Med. Imag.*, vol. 29, no. 1, pp. 185–195, Jan. 2010.
- [33] B. Antal and A. Hajdu, "An ensemble-based system for microaneurysm detection and diabetic retinopathy grading," *IEEE Trans. Biomed. Eng.*, vol. 59, no. 6, pp. 1720–1726, Jun. 2012.